



Photocatalytic oxidation of gas-phase Hg^0 on the exposed reactive facets of BiOI/BiOIO₃ heterostructures

Ruixing Zhou^a, Jiang Wu^{a,*}, Jing Zhang^a, Huan Tian^a, Pankun Liang^a, Tao Zeng^b, Ping Lu^c, Jianxing Ren^a, Tianfang Huang^a, Xiao Zhou^a, Pengfei Sheng^a

^a College of Energy and Mechanical Engineering, Shanghai University of Electric Power, Shanghai 200090, China

^b Shanghai Key Laboratory of Engineering Materials Application and Evaluation, Shanghai Research Institute of Materials, Shanghai 200050, China

^c School of Energy and Mechanical Engineering, Nanjing Normal University, Nanjing 210042, China

ARTICLE INFO

Article history:

Received 28 May 2016

Received in revised form 16 October 2016

Accepted 8 November 2016

Available online 9 November 2016

Keywords:

Photocatalytic oxidation

Hg^0

BiOIO₃

BiOI

Heterostructure

ABSTRACT

Hetero layered BiOI/BiOIO₃ composites were fabricated by a simple hydrothermal method. The prepared BiOI/BiOIO₃ heterostructures were characterized and evaluated for gas-phase Hg^0 oxidation. The photocatalytic activity of the BiOI/BiOIO₃ heterostructures was detected under LED light and UV irradiation. Meanwhile, the cycle experiments were carried out to certify the stability of BiOI/BiOIO₃ composites. The results showed that BiOI/BiOIO₃ photocatalysts were of excellent photocatalytic ability with great efficient in oxidizing Hg^0 . The Hg^0 removal efficiency reached up to 98.53% and 100% under LED light and UV irradiation respectively when the mole ratio of BiOI/BiOIO₃ was 3:1. The photocatalytic reaction mechanism was elaborated in detail.

© 2016 Published by Elsevier B.V.

1. Introduction

Mercury emitted from coal combustion seriously damages to the environment, and as a toxic pollutants, it can harm to human health through the food chain biological accumulation. United States Environmental Protection Agency (EPA) survey has concluded that coal fired power plant is the largest source of mercury emissions, accounting for 1/3 of anthropogenic mercury emissions [1]. And the control of mercury emissions has caused enough attention [2]. China's ministry of environmental protection issued a new national regulation for coal-fired power station in 2011, in which mercury emission controlling standard was mentioned for the first time, and the limiting value of mercury emission is less than 0.03 mg/m³ [3]. Hg exists in three chemical forms in coal combustion flue gas: elemental mercury (Hg^0), oxidized mercury (Hg^{2+}), and particle-bound mercury (Hg^p) [4]. Mercury removal from flue gas largely depends on the form of mercury in the flue gas. Hg^{2+} is water-soluble, so it can be removed by wet scrubbers and the removal efficiency can reach up to 90% [5,6]. Hg^p can be easily removed by electrostatic precipitator (ESP) or fabric filter (FF) [7]. But it is difficult for the existing air pollution control devices (APCDs) to remove

Hg^0 because of its volatility, insolubility and chemical stability [5], so it is a great challenge to remove Hg^0 from flue gas at the coal combustion power stations. The key is to oxidize Hg^0 into Hg^{2+} in the flue gas. Recently, the research progress of photocatalytic oxidation removing Hg^0 gives us a new perspective [8]. Compared with other methods, photocatalytic oxidation method is of the highest efficiency without secondary pollution and it has recyclable characteristics. Therefore, Hg^0 removal from coal combustion flue gas has great potential development [9].

Photocatalytic in the direct use of solar energy to solve the two major issues of environmental pollution and energy shortage shows potential application prospects. In all of this, semiconductor photocatalysts have been applied to energy conversion, photocatalysis remediation and organic synthesis [10–14]. The traditional TiO₂ photocatalyst is widely recognized semiconductor for photocatalytic oxidation because of its high chemical stability, high specific surface area, low cost, strong oxidation ability and photocatalytic activity [15]. However, TiO₂ can only be excited by ultraviolet (UV) irradiation, which accounts for merely about 4% of the total solar radiation, what's more, the rapid recombination of photogenerated electron-hole pairs (e^- – h^+) causes poor quantum yield [16]. Hence many researchers have tried to improve the photocatalytic oxidation under visible light, and to improve the efficiency of photocatalytic oxidation, which included metal or non-metal ion doping [17–20], surface modification [17,18], combining

* Corresponding author at: No. 2103 Pingliang Road, Shanghai 200090, China.
E-mail address: wjcf2002@sina.com (J. Wu).

with other semiconductors or metal oxides [19,20], etc. However, to some extent, these methods have not achieved the desired photocatalytic efficiency of mercury removal.

Bi-based layered semiconductors were found to possess a high photocatalytic activity [21]. The heterolayered BiOI/O₃ possesses an excellent photocatalytic activity among all of these Bi-based layered semiconductors, which is mainly due to the internal polar field and the heterolayered structure. Both features can effectively separate the e^- – h^+ at the BiO₆ and IO₃ pyramids [22]. In our previous work [23], the pristine BiOI/O₃ photocatalyst was fabricated and studied the effect of pH value on its morphology and crystal structure, and we discussed its photocatalytic performance. However, the relatively wide band gap (3.13 eV) of BiOI/O₃ reduces its photoactivity under visible light. So we used BiOI with a narrow band gap (1.75 eV) to dope with BiOI/O₃ to narrow the band gap of BiOI/BiOI/O₃ compounds which can also fabricate the heterostructures, increasing the response to visible light region and separating the photogenerated e^- – h^+ . The photoactivity experiments of BiOI/BiOI/O₃ compounds were verified under ultraviolet (UV) light and visible light to remove mercury. Related research has been conducted in previous work [24], in which we used Bi(NO₃)₃·5H₂O and KIO₃ as the raw materials and added carbon spheres (CSs) into the solution to reduce I⁵⁺ to I[−] directly, resulting in the formation of BiOI and carbon-doped simultaneously. In the previous work, we mainly emphasized the importance of carbon. The doped carbon element and produced BiOI can bring dramatic changes in their structural, optical, electronic and chemical properties, and the CSs acted as a photosensitizer. However the fabrication process was relatively cumbersome. In this study, we improved the fabrication process, which was very simple and was of low cost. We studied the effects of exposed reactive facets on photocatalytic activity and discussed the mechanism of mercury removal from two aspects of band gap and internal structure of the sample. The physical and chemical properties of the as-prepared BiOI/BiOI/O₃ compounds were characterized with a series of techniques, such as UV–vis DRS, PL, XRD, XPS, SEM and TEM. The as-prepared BiOI/BiOI/O₃ compounds were applied to photocatalytic oxidation of gaseous elemental mercury under ultraviolet (UV) light and visible light.

2. Experimental

2.1. Chemicals and materials

Bismuth nitrate pentahydrate, Potassium iodate, Potassium iodide, acetic acid were all obtained from Guoyao Chemical Reagent Co. Ltd. All solutions were prepared with deionized water and all chemicals used in this study were analytical grade and were used without further purification.

2.2. Preparation of BiOI/BiOI/O₃ photocatalyst

BiOI/O₃ was prepared by a simple hydrothermal method. In a typical procedure, 0.485 g of Bi(NO₃)₃·5H₂O was dissolved into 80 mL H₂O, and stirred vigorously for 30 min. Then, 0.214 g of KIO₃ was added into the above aqueous and continuously stirred for 10 min. The obtained suspension was then hydrothermally treated at 150 °C for 6 h. Finally, the BiOI/O₃ product was collected and dried at 60 °C for 12 h.

BiOI/BiOI/O₃ heterostructured nanocomposites were synthesized by a chemical precipitation method at room temperature. A certain amount of Bi(NO₃)₃·5H₂O was dissolved in 80 mL H₂O containing 9 mL of acetic acid, and 0.48 g of BiOI/O₃ was added into the above aqueous solution and stirred for 10 min. Then, 30 mL aqueous solution containing stoichiometric amount of KI was added drop-

wise into the solution and stirred for 2 h. After the stirring was completed, the resulted suspension was aged for 2 h. Finally, the resulted products were collected by filtration, washed with water and ethanol for several times and dried at 60 °C to obtain the final products. Depending on the molar ratio of BiOI/O₃ to BiOI (1:0, 6:1, 3:1, 1:1, 0:1), different nanocomposites can be synthesized and named as BiOI/O₃, B-6, B-3, B-2, B-1 and BiOI respectively.

2.3. BiOI/BiOI/O₃ photocatalyst characterization

The crystal phases of the samples were analyzed by X-ray diffraction (XRD) with Cu K α radiation (BRUKER D8 ADVANCE Diffractometer, Germany). The UV–vis diffuse reflectance spectra (UV–vis DRS) was recorded at room temperature in the range of 250–1000 nm using a UV–vis spectrophotometer (SHIMADZU UV-3600 Plus, Japan) equipped with an integrating sphere, using BaSO₄ as the reflectance sample. The photoluminescence (PL) spectra of the materials were acquired on a fluorescence spectrophotometer (SHIMADZU RF5301, Japan) at an excitation wavelength of 315 nm. N₂ physisorption isotherms were determined at liquid nitrogen temperature (−195 °C) using a Micromeritics ASAP 2020 instrument. Specific surface areas were calculated from the N₂ adsorption data according to the Brunauer–Emmett–Teller (BET) method using P/P₀ values in the range 0.05–0.2 [25]. Samples were degassed at 80 °C under vacuum for 6 h prior to the N₂ physisorption measurements. The morphologies of the catalysts were determined using a scanning electron microscope (SEM, Phillips XL-30 FEG/NEW), and transmission electron microscopy (TEM) and high-resolution transmission electron microscopy (HRTEM) images were used to further analyze the morphology and crystallinity of the products on a Phillips Model CM200 transmission electron microscope. X-ray photoelectron spectroscopy (XPS) with Al K α X-ray (h ν = 1486.6 eV) radiation operates at 250 W (PHI5300, USA) was used to investigate the surface properties.

2.4. Measurement of photoactivity

The photocatalytic activity was evaluated using a laboratory scale test system, which was similar to that used in our previous studies [23]. The compressed air out of the air compressor was divided into two branches, the atmospheric air humidity was 0.6%, the flow rate was controlled by two mass flow meters (CS200 type), and the total flow rate was maintained at 1.2 L min^{−1}. One of the air streams with a flow rate of 0.2 L/min passed through the Hg⁰ permeation tube to introduce Hg⁰ vapor to the system. The mercury permeation tube was placed in a U-shape glass tube, which was immersed in a water bath at constant temperature (55 °C) to ensure a constant Hg⁰ permeation rate. The other air stream was the main branch, which was of a 1.0 L min^{−1} flow rate. Two shares of gas mixed in the mixing tank. The gas out of the mixing tank through adjustment of the three-way valve and the two-way valve respectively into the photocatalytic reactor and the bypass, and the gas after reaction or the gas of bypass passed silica gel into the LUMEX type of gas-line mercury analyzer to measure the gas phase concentration of Hg⁰. Finally, the gas got through the exhausted gas absorption bottle and was emitted.

The Hg⁰ test was carried out with the catalyst loaded on the glass fabric under the light irradiation. The as-prepared samples were dissolved in alcohol, then shocked with ultrasonic for 30 min. After that, the glass fabric attached with photocatalytic was dried in an oven at around 80 °C for 15 min. The above process was repeated for three times so that sufficient photocatalysts were loaded on the glass fabric, then it was put into the photocatalytic reactor developed by ourselves [26]. The loading of catalyst was about 50 mg.

In order to describe this phenomenon in detail, the Hg^0 removal efficiency was defined as following:

$$\eta_{\text{Hg}} = \frac{\text{Hg}_{\text{inlet}}^0 - \text{Hg}_{\text{outlet}}^0}{\text{Hg}_{\text{inlet}}^0} \times 100\%$$

where $\text{Hg}_{\text{inlet}}^0$ ($\mu\text{g}/\text{m}^3$) represented Hg^0 at the inlet of reactor, and $\text{Hg}_{\text{outlet}}^0$ ($\mu\text{g}/\text{m}^3$) out represented Hg^0 at the outlet of the reactor.

3. Results and discussions

3.1. XRD analysis

The XRD patterns of the as-prepared $\text{BiOI}/\text{BiOI}_3$ catalysts were depicted in Fig. 1. The XRD diffraction peaks of BiOI_3 were in good agreement with the orthorhombic BiOI_3 (ICSD # 262019). The obtained BiOI sample was well crystallized and can be indexed to tetragonal structure for BiOI (JCPDS file no.73-2062). The (010) and (040) peaks of $\text{BiOI}/\text{BiOI}_3$ heterostructures offset to a large angle to a certain extent compared to that of the pure BiOI_3 , which is because the samples shifted towards the long wavelength. The enlarged spectrum of (010) peaks were shown in Fig. 1b, the intensity of (010) peak first gradually increased from B-6 to B-3 and then decreased from B-3 to B-1 with the increase of the content of BiOI , i.e., the intensity of (010) peak was the strongest when the mole ratio of $\text{BiOI}/\text{BiOI}_3$ was 3:1. We can see from the enlarged XRD spectrum (Fig. 1c), the intensity of (040) peak of BiOI_3 was the strongest when the mole ratio of $\text{BiOI}/\text{BiOI}_3$ compounds also was 3:1. The Fig. 1d revealed the ratio of (040)/(002) of $\text{BiOI}/\text{BiOI}_3$ compounds, which showed the same trend that B-3 possessed the largest intensity ratio value of (040)/(002). It verified that B-3 possesses the highest exposure {010} facet, while excessive BiOI products may cover the {010} facet of BiOI_3 , conversely reducing the exposure ratio [27]. Therefore the B-3 sample may have the highest photocatalytic activity.

3.2. Optical properties

The optical properties of the $\text{BiOI}/\text{BiOI}_3$ compounds were confirmed by UV–vis diffuse reflectance spectroscopy. The Fig. 2a revealed that the as-prepared $\text{BiOI}/\text{BiOI}_3$ compounds owned an excellent visible light absorption performance, while the pure BiOI_3 and BiOI can be excited before 380 nm and 700 nm respectively. For a semiconductor, the band gap energy is described by the following equation [28]:

$$\alpha h\nu = A(h\nu - E_g)^{n/2},$$

where α is the absorption coefficient, $h\nu$ is the photon energy, A is a constant and E_g is the band gap. Both of BiOI_3 and BiOI are indirect transition semiconductor, so for them, $n = 4$. From the $(\alpha h\nu)^{1/2}$ vs $h\nu$ plot (Fig. 2b), the band gap energies of BiOI_3 and BiOI are 3.13 eV and 1.75 eV respectively. In the same way, the band gap energies of B-6, B-3, B-2 and B-1 are 3.04 eV, 2.72 eV, 2.61 eV and 1.86 eV respectively. The valence band-edge potential of a semiconductor can be calculated by the empirical equation $E_{\text{VB}} = \chi - E^e + 0.5E_g$ [29], where χ is the electronegativity of the semiconductor atoms, E^e is the energy of free electrons on the hydrogen scale (about 4.5 eV), and E_g is the band gap energy of semiconductor. The CB bottom E_{CB} can be determined by $E_{\text{CB}} = E_{\text{VB}} - E_g$. The χ value of BiOI_3 is about 7.04 eV, so the E_{VB} is calculated to be 4.11 eV, and E_{CB} is calculated to be 0.98 eV. For BiOI , the χ value is about 5.99 eV, hence the E_{VB} is calculated to be 2.37 eV, and E_{CB} is calculated to be 0.62 eV.

Table 1

The BET surface areas and the Hg^0 removal efficiency of the samples.

Products	BET surface area (m^2/g)	Removal efficiency(LED) (%)
BiOI	2.1517	12.45
B-1	14.4314	61.35
B-2	15.9582	80.71
B-3	14.2358	98.53
B-6	13.4529	91.95
BiOI_3	27.7027	59.31

3.3. Photoluminescence spectra

PL is a powerful characterization method for detecting the separation efficiency of $e^- - h^+$ [30,31]. The lower intensity of the PL peak, the higher separation efficiency of $e^- - h^+$ [30,31]. With an excitation wavelength at 315 nm, the PL spectra of the as-prepared samples was presented in Fig. 3. It can see that all samples had emission peaks at about 460 nm, and the emission peak strengths of $\text{BiOI}/\text{BiOI}_3$ compounds were lower than that of the pure BiOI_3 and BiOI , which demonstrated that the $\text{BiOI}/\text{BiOI}_3$ compounds were favorable for the separation of the $e^- - h^+$. Among all the emission peaks, the emission peak of B-3 was the weakest, so it can be speculated that the photocatalytic activity of B-3 was the best.

3.4. BET analysis

The specific surface area is usually closely related to the activity of photocatalyst, and generally the larger the specific surface area, the more active sites exposed, the more conducive to the photocatalytic reaction. The specific surface areas and Hg^0 removal efficiencies of the as-prepared samples were listed in Table 1. The specific surface areas of $\text{BiOI}/\text{BiOI}_3$ compounds were almost the same sizes, but the Hg^0 removal efficiencies of $\text{BiOI}/\text{BiOI}_3$ compounds differed greatly. The B-3 had the highest photocatalytic activity, whereas the specific surface area was not the largest, so the specific surface areas of $\text{BiOI}/\text{BiOI}_3$ compounds were not the major factor that affects the photocatalytic properties[22]. We assumed the exposed reactive facets of the (010) facets of BiOI_3 and the {001} facets of BiOI were the dominant factors that affect the photocatalytic properties. The Fig. 4 revealed that nitrogen adsorption-desorption isotherms were all IV type and the existed hysteresis loop extended from $P/P_0 = 0.6$ to $P/P_0 = 1$, demonstrating that the as-prepared $\text{BiOI}/\text{BiOI}_3$ compounds were mesoporous and macroporous materials, and that the pore structure was mainly formed by the stacking of nano sheets, which was consistent with the SEM and TEM results.

3.5. $\text{BiOI}/\text{BiOI}_3$ SEM and TEM analysis and its formation mechanism

The morphologies of BiOI_3 , BiOI and $\text{BiOI}/\text{BiOI}_3$ compounds were explored by SEM and TEM. The Fig. 5a showed that BiOI approximated to rectangular nanosheet with smooth surface. The Fig. 5b revealed that the structure of BiOI_3 was also smooth nanosheet. The Fig. 5c and d were respectively corresponding to the low and high magnification SEM spectrum of B-3, which indicated the BiOI_3 and BiOI nanosheets stacking together in a regular and repeating pattern. The Fig. 5e and f verified the neat and smooth surfaces of the pristine BiOI_3 and BiOI , and the diameters of BiOI_3 and BiOI were 100 nm and 200 nm respectively. The lattice fringe can be clearly seen in HRTEM spectrum through Fig. 5g and h, and the lattice fringes with the interplane space of 0.287 nm corresponded to (002) plane of BiOI_3 . Combined with the XRD spectrum, it can be explored that the dominant exposed reactive facet of BiOI_3 may be {010} facet. The lattice fringes of

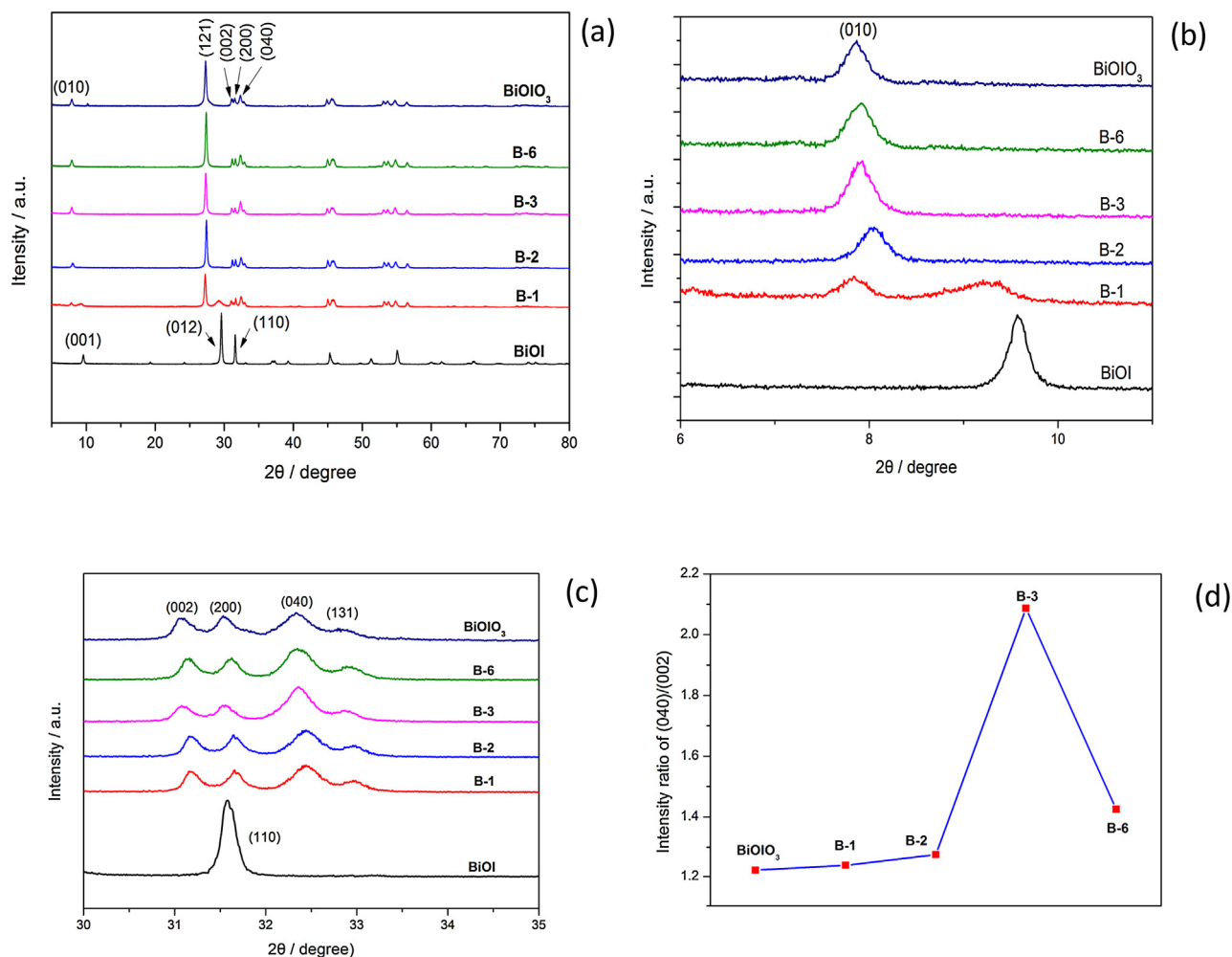


Fig. 1. XRD pattern of the BiOI₃, BiOI and BiOI/BiOI₃ heterostructures.

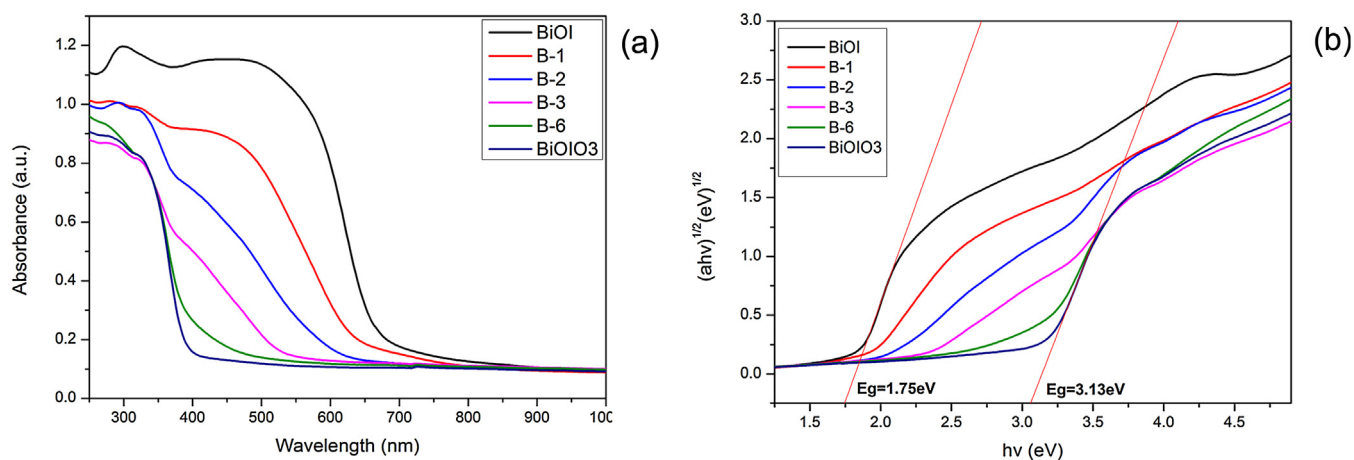


Fig. 2. (a) UV-vis DRS of the as-prepared samples and (b) band gap of BiOI₃, BiOI and BiOI/BiOI₃ heterostructures.

the interplane space of 0.280 nm corresponded to the (110) plane of BiOI. According to the (001) peak of XRD, the major exposed reactive facet of BiOI was {001} facet. The exposed {001} facets of BiOI can promote the photocatalytic activity, which was due to the effective separation of photogenerated e^- – h^+ on {001} facets [27]. The BiOI were formed on the surface of BiOI₃, which indi-

cated that the BiOI/BiOI₃ heterostructures were synthesized and the BiOI/BiOI₃ layers contacted intimately.

The BiOI/BiOI₃ formation mechanism was shown in Fig. 5i. The {010} facets of BiOI₃ were first synthesized. the {010} facets of BiOI₃ were formed by the oxygen atoms, and the (Bi₂O₂)²⁺ layer connected the (IO₃)⁻ layer to generate BiOI₃. As the atoms arrangement of {001} facets of BiOI was similar to that of the {010}

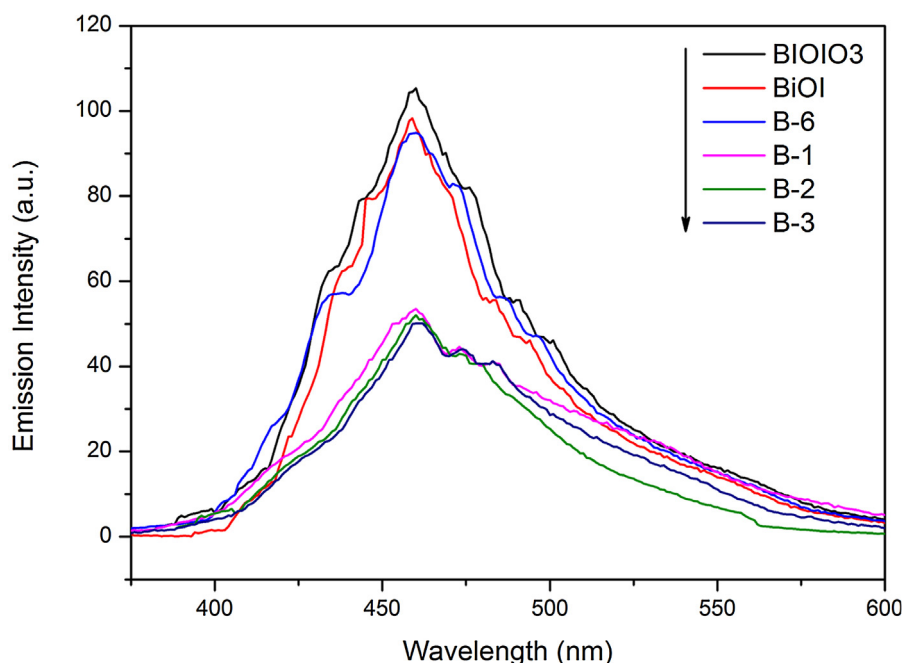


Fig. 3. Photoluminescence spectra of BiOIO₃, BiOI and BiOI/BiOIO₃ compounds.

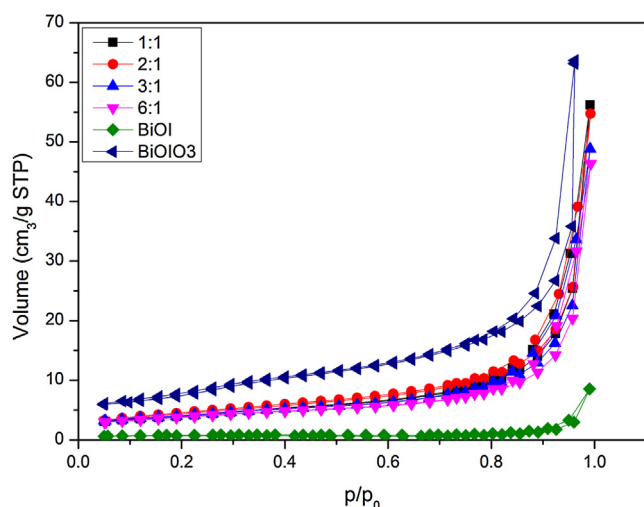


Fig. 4. Nitrogen adsorption–desorption isotherms.

facets of BiOIO₃, the {001} facets of BiOI grew along the {010} facets of BiOIO₃, and the I slabs with the [Bi₂O₂] sheets stacked together to form [Bi₂O₂I₂] by nonbonding interaction [32]. Due to the sharing of oxygen atoms of {010} facets and {001} facets, which can increase contacting areas and intimate interface, the distinctive structure can effectively promote the transfer of photogenerated e[−]–h⁺ between the BiOI/BiOIO₃ heterostructures [32].

3.6. XPS analysis

The surface compositions of the samples were analyzed by X-ray photoelectron spectroscopy (XPS), shown as Fig. 6. It can be seen from Fig. 6a that the as-prepared samples contained the elements of I, O, Bi and C. The peak for C 1s (284.8 eV) was just attributed to the adventitious carbon. The Fig. 6b indicated that B-3 displayed two sets of I 3d peaks, and the two strong peaks at around 638.4 eV and 627.2 eV were assigned to I 3d_{5/2} and I 3d_{3/2} states of I⁵⁺, whereas the other two strong peaks at about 633.2 eV and 621.4 eV were

attributed to I 3d_{3/2} and I 3d_{5/2} states of I[−] [22,27], and the I⁵⁺ and I[−] ions were in BiOIO₃ and BiOI respectively. The Bi atoms exhibited the peaks at 164.8 eV and 158.8 eV (Fig. 6c), corresponding to Bi 4f_{2/5} and Bi 4f_{2/7}, which indicated that the Bi atoms in B-3 were in the form of Bi³⁺. Moreover, the O 1s region can be indexed to the peak at 532.8 eV (Fig. 6d), and the peak belonged to O^{2−} in Bi–O bands and I–O bands. Compared with the pristine BiOIO₃ and BiOI, the binding energy of I, Bi and O in BiOI/BiOIO₃ heterostructures (B-3) all shift towards high binding energy, which indicated that the interaction between BiOIO₃ and BiOI at the composite interface did occur, and the XPS spectrum can also confirm the coexistence of BiOIO₃ and BiOI in BiOI/BiOIO₃ composites and the effective composites were formed between the two kinds of the pristine phase materials.

3.7. Photocatalytic properties

The photocatalytic activities of the as-prepared samples were estimated by photocatalytic oxidation of Hg⁰. The 24 W LED light was used, whose wavelength was 420 nm, as the visible light source. Each experiment was carried out for around 7200 s, the photocatalytic oxidation of Hg⁰ was investigated under dark (1000 s), visible light irradiation (3500 s) and UV irradiation (2700 s) respectively (Fig. 7). Under visible light irradiation (LED light), the Hg⁰ removal efficiencies of pristine BiOIO₃ and BiOI were only 59.31% and 12.35% respectively, whereas BiOI/BiOIO₃ heterostructures displayed remarkable photocatalytic activity for removing Hg⁰, and the Hg⁰ removal efficiency first increased with the increase of the content of BiOI, and then decreased with the increase of the content of BiOI. The Hg⁰ removal efficiency was the highest when the mole ratio of BiOI/BiOIO₃ compounds was 3:1 (B-3), reaching about 98.53%, which was really consistent with the characterization results. However, under UV irradiation, the photocatalytic activity of B-3 was not the highest, instead, the photocatalytic oxidation efficiency of B-6 was the highest and it even can reach 100%. The BiOI almost had no photocatalytic activity, this may be due to the instability of BiOI. The BiOI was constituted by a layered structure of alternate [Bi₂O₂] sheets and double I slabs, stacking together by the nonbonding interaction [32], whose bonding force was relatively

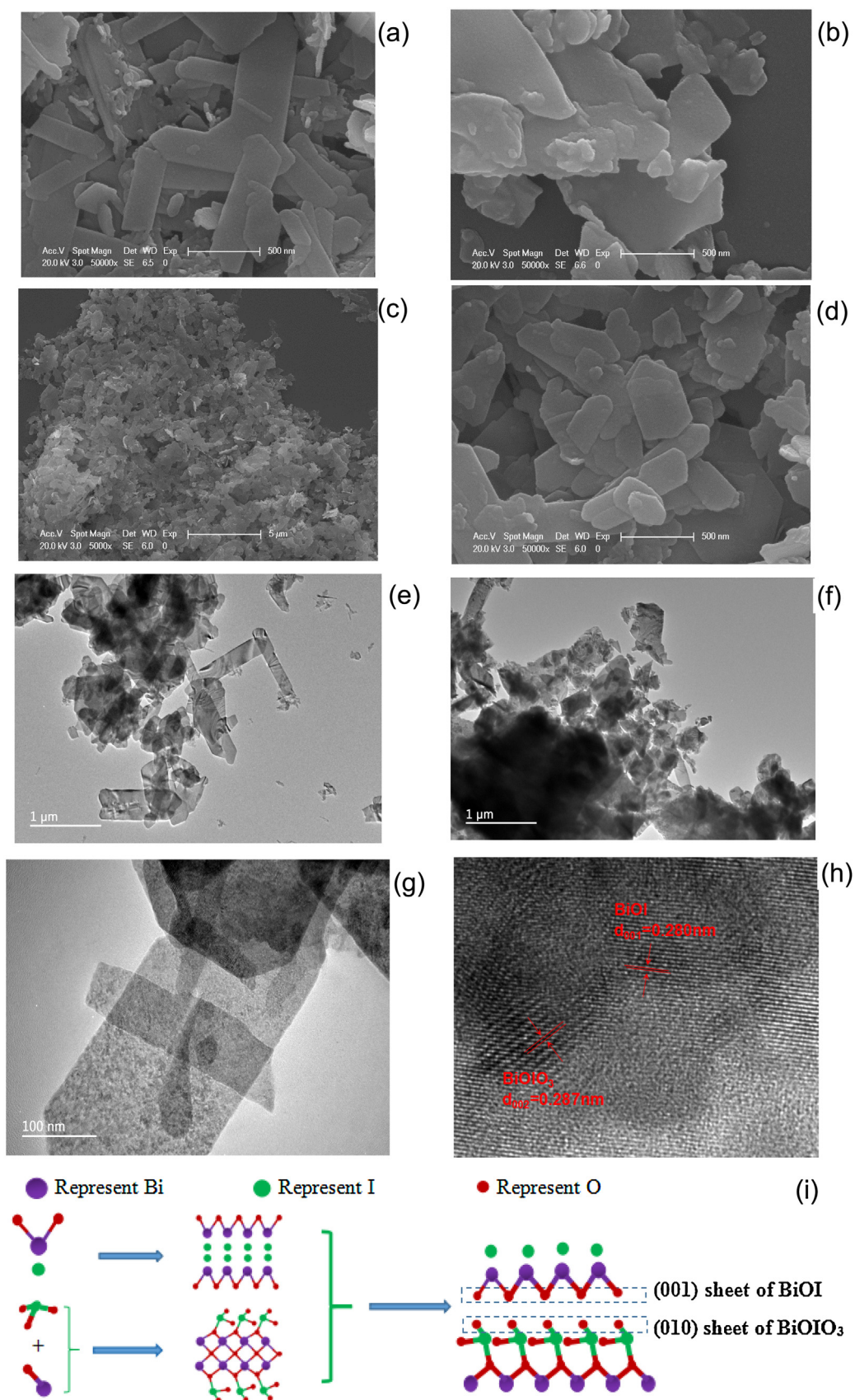


Fig. 5. The SEM images of BiOI (a); BiOIO₃ (b); B-3 (c, d), TEM images of BiOIO₃ and BiOI (e, f), HRTEM images of B-3 (g, h) and the formation mechanism (i).

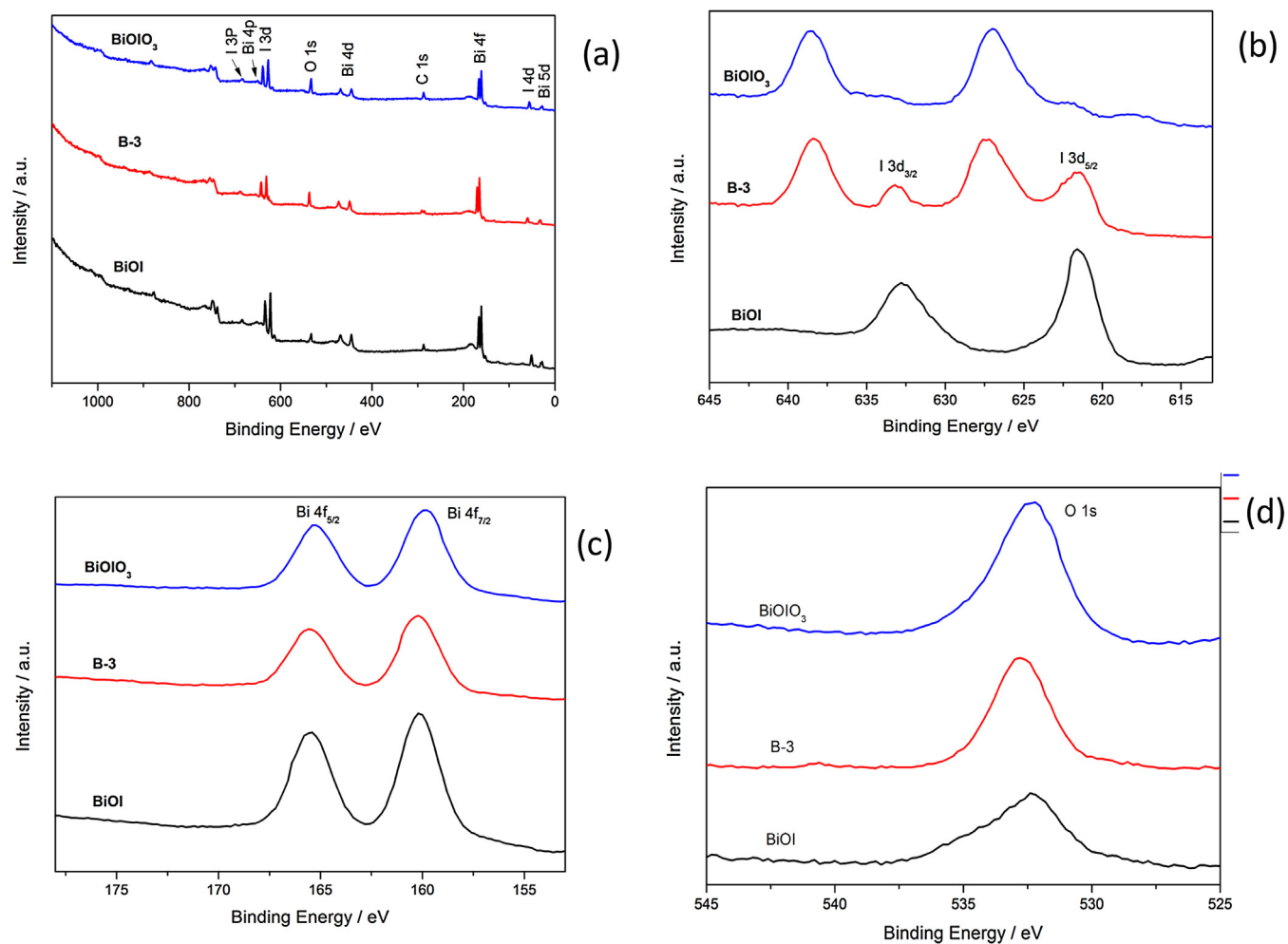


Fig. 6. XPS spectrum of BiOIO₃, BiOI and the B-3: survey XPS spectrum (a), I 3d (b), Bi 4f (c) and O 1s (d).

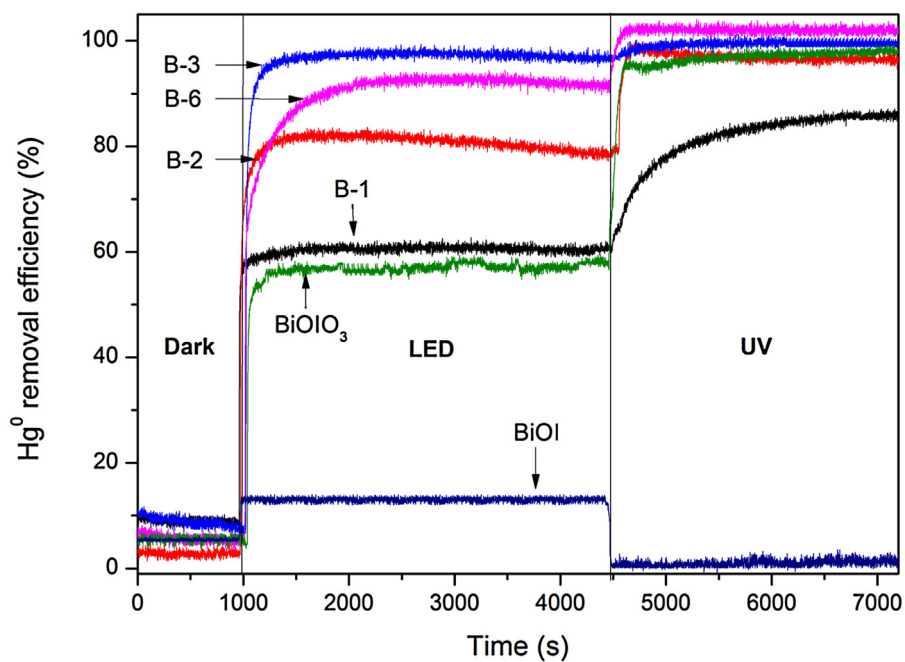


Fig. 7. Removal efficiencies of Hg⁰ for the samples under dark, LED and UV light irradiation.

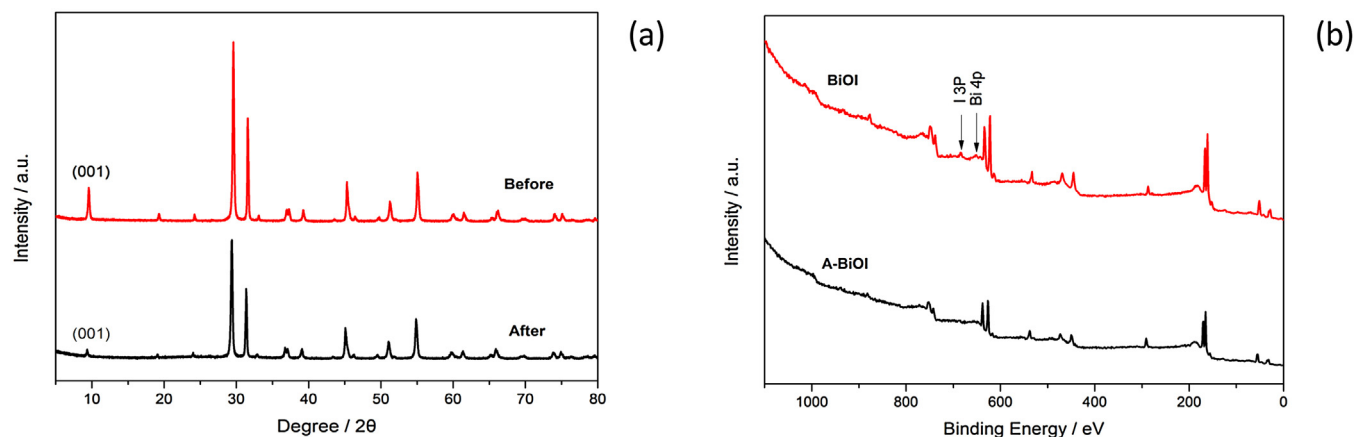


Fig. 8. The XRD and XPS spectrum of BiOI before and after the reaction.

weak, so the layered structure would easily dissociated along the (001) direction. As shown in Fig. 8a, the (001) peak of the reacted BiOI weakened much compared to that of the pristine BiOI. The {001} facet of BiOI is the dominantly exposed reactive facet, which may be the reason why BiOI has no photocatalytic activity under UV light. The XPS spectra of pristine BiOI and reacted BiOI were shown as Fig. 8b, showing that every peak had somewhat weakness and even disappeared, such as the I 3p and Bi 4p, which is consistent with the XRD results shown in Fig. 8a.

3.8. Stability of BiOI/BiOIO₃ heterostructures

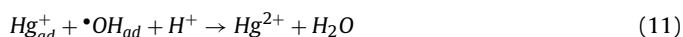
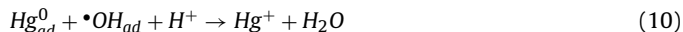
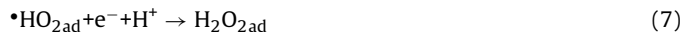
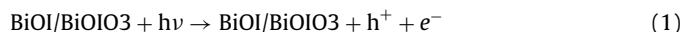
Compared to the photocatalytic activity, the stability of photocatalyst is also very important. To study the stability of the B-3 photocatalyst, recycle experiments of Hg⁰ removal were conducted and each group was carried out for about 2500 s under LED light irradiation (Fig. 9a), and Hg⁰ removal efficiency of B-3 was explored for consecutive 7 cycles. In each cycle, the quartz glass coated with B-3 photocatalyst was first exposed to LED light. The LED light was turned off after the exposure to LED light about 2500s, and then the next cycle experiment was carried out when the Hg⁰ concentration reached the certain stable value. The following cycle experiment was conducted as the above procedures. The Hg⁰ removal efficiency can also reach 98.5% after consecutive 7 cycles, revealing that the B-3 photocatalyst possesses excellent and stable photocatalytic activity for removing Hg⁰. The structures of B-3 photocatalyst before and after 7 consecutive cycle experiments were characterized by the XRD analysis, as exhibited in Fig. 9b, the dominant (001) peak substantially unchanged, which indicates that the B-3 photocatalyst still holds the stable chemical structure even after 7 cycle experiments.

3.9. Photocatalytic reaction mechanisms

The photocatalytic activities of the as-prepared BiOI/BiOIO₃ heterostructures are higher than that of a single component, and the formed heterostructures can effectively promote the separation of the e⁻ and h⁺. The transfer direction of e⁻ and h⁺ between the semiconductors directly related to the band structure of the semiconductors. The Fermi level of p-type semiconductor BiOI is near the valance band, whereas the Fermi level of n-type semiconductor BiOIO₃ is near the conduction band. When a p-n junction is formed between the BiOIO₃ and BiOI, the Fermi level of p-type semiconductor BiOI and n-type semiconductor BiOIO₃ are first to achieve the balance, meanwhile the valance and conduction band positions of BiOI move towards the more negative electronegativity, and the valance and conductor bands position of BiOIO₃ move towards the

more positive electronegativity. As shown in Fig. 10a, under visible light irradiation, the BiOI is excited to yield the e⁻ and h⁺, while the conduction position of BiOI is more negative than that of BiOIO₃, so the e⁻ transfer from the conduction band of BiOI to the conduction band of BiOIO₃, however the h⁺ are left in the valance band of BiOI. The energetic e⁻ transfer to the conduction band of BiOIO₃ and react with O₂ absorbed on the surface of the catalyst to generate O₂⁻. The h⁺ left on the valance band of BiOI also can adsorb the OH⁻ or H₂O on the surface of catalyst to form ·OH, and then the high activity ·OH and O₂⁻ photocatalytically oxidize Hg⁰ into Hg²⁺. What's more, because of the internal polar field in the pristine BiOIO₃ and BiOI, the e⁻ and h⁺ migrate to the composite interface of the {010} facets of BiOIO₃ and the {001} facets of BiOI. There is an internal polar field perpendicular to the nano sheet in BiOI and an internal polar field parallel to the nano sheet in BiOIO₃ [33]. As shown in Fig. 10b, the h⁺ in BiOI migrate from the interior to the {001} facets due to the internal polar field perpendicular to the nano sheet, while the h⁺ photogenerated at IO₃ pyramid and BiO₆ pyramid in BiOIO₃ tend to diffuse around the {010} facets due to the horizontal internal polar field and the e⁻ generated at IO₃ pyramid and BiO₆ pyramid transfer to Bi 6P CB bottom. In this progress, the h⁺ migration along the horizontal direction on the {010} facets of BiOIO₃ is shorter than that of other directions so that it is easier to contact the materials. As being reported on most of literature [34–36], the h⁺ and ·O₂⁻ are both the main species responding to the oxidation. In this work, because the h⁺ react with H₂O or OH⁻ to produce the ·OH, and the ·OH oxidize Hg⁰ into Hg²⁺, so the essential species responding to the oxidation is still h⁺.

The Photocatalytic oxidation reaction can be described as the following Eqs. (1)–(11) [26,37–39].



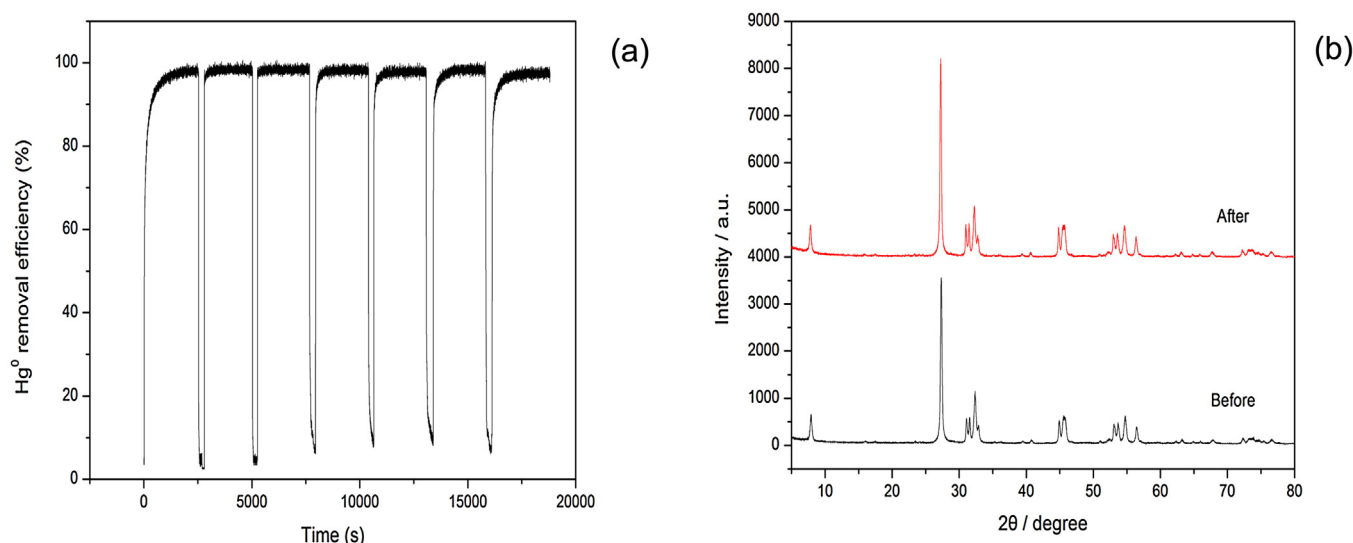


Fig. 9. Repeated photocatalytic activity of B-3 (a) and the XRD comparison spectrum (b).

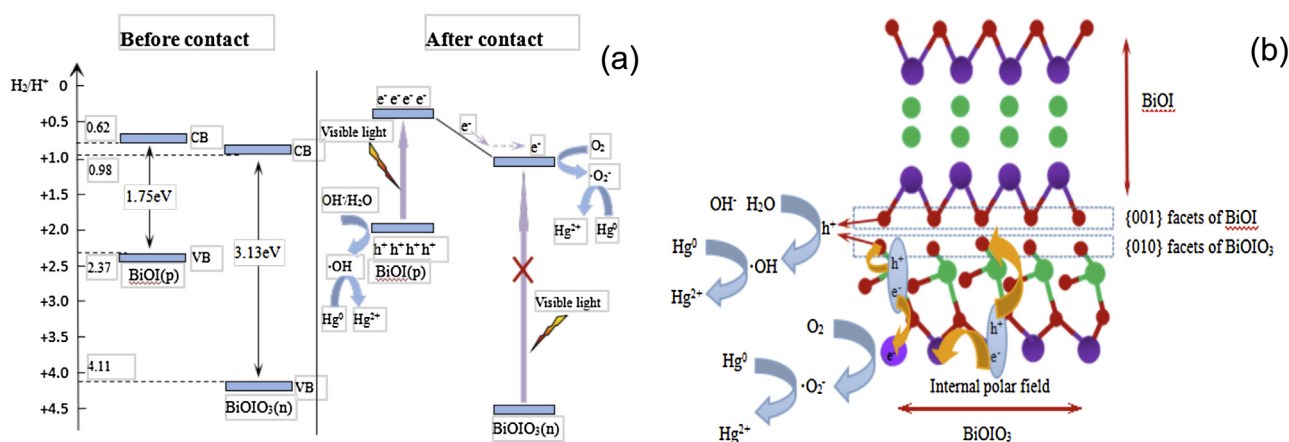


Fig. 10. (a) Mechanism of separation of photo electron-holes. (b) Schematic diagram of composite interface structure of BiOI/BiOIO₃ composites.

4. Conclusions

- 1) The BiOI/BiOIO₃ heterostructures were fabricated by a simple hydrothermal synthesis method, and their photocatalytic activities were verified by removing Hg⁰ in flue gas. The BiOI/BiOIO₃ heterostructures possess more superior photocatalytic activity compared to the conventional photocatalysts.
- 2) The dominant active facets of the as-prepared BiOI/BiOIO₃ nano-composite photo-catalyst are the {010} facets of BiOIO₃ and the {001} facets of BiOI. The {010} facets and the {001} facets shared interfacial oxygen atoms, which shaped a large contact area and intimate contact. What's more, the BiOI/BiOIO₃ heterostructures can efficiently separate the photogenerated electrons and holes, being confirmed by the PL spectra and the photocatalytic results.
- 3) The pure BiOI was not stable under UV light irradiation, but the BiOI/BiOIO₃ heterostructures were much more stable, which has been confirmed by XRD spectra and cycle experiments. The as-prepared BiOI/BiOIO₃ heterostructures can be applied to photocatalysis remediation on environmental pollution.

Acknowledgments

This work was partially sponsored by NSF (Natural Science Foundation, 21237003, 50806041, 51106133, 51606115),

Shanghai Science and Technology Development (15dz1200703, 11dz1203402, 15110501000).

References

- [1] Sh.Sh. Chen, H.Ch. Hsi, Sh.H. Nian, Ch.H. Chiu, Synthesis of N-doped TiO₂ photocatalyst for low-concentration elemental mercury removal under various gas conditions, *Appl. Catal. B* 160–161 (2014) 558–565.
- [2] A.A. Presto, E.J. Granite, Survey of catalysts for oxidation of mercury in flue gas, *Environ. Sci. Technol.* 40 (2006) 5601–5609.
- [3] Emission standard of air pollutants for power plants, GB 13223–2011.
- [4] C.E. Romero, Y. Li, H. Bilirgen, N. Sarunac, E. Levy, Modification of boiler operating conditions for mercury emissions reductions in coal-fired utility boilers, *Fuel* 85 (2006) 204–212.
- [5] Y. Li, P.D. Murphy, C.Y. Wu, K.W. Powers, J.C.J. Bonzongo, Development of silica/vanadia/titania catalysts for removal of elemental mercury from coalcombustion flue gas, *Environ. Sci. Technol.* 42 (2008) 5304–5309.
- [6] Dennis Y. Lu, David L. Granatstein, Donald J. Rose, Study of mercury speciation from simulated coal gasification, *Ind. Eng. Chem. Res.* 43 (2004) 5400–5404.
- [7] E.J. Granite, H.W. Pennline, Photochemical removal of mercury from flue gas, *Ind. Eng. Chem. Res.* 41 (2002) 5470.
- [8] S.H. Jeon, Y. Eom, T.G. Lee, Photocatalytic oxidation of gas-phase elemental mercury by nanotitanosilicate fibers, *Chemosphere* 71 (2008) 969–974.
- [9] M.R. Hoffmann, S.T. Martin, W. Choi, D.W. Bahnemann, Environmental applications of semiconductor photocatalysis, *Chem. Rev.* 95 (1995) 69–96.
- [10] Q.J. Xiang, J.G. Yu, Photocatalytic activity of hierarchical flower-like TiO₂ superstructures with dominant {001} Facets, *Chin. J. Catal.* 32 (2011) 525–531.
- [11] X.C. Wang, S. Blechert, M. Antonietti, Polymeric graphitic carbon nitride for heterogeneous photocatalysis, *ACS Catal.* 2 (2012) 1596–1606.

- [12] S.W. Cao, J.G. Yu, G-C3N4-based photocatalysts for hydrogen generation, *J. Phys. Chem. Lett.* 5 (2014) 2101–2107.
- [13] C. Zhou, Y. Zhao, L. Shang, Y. Cao, L. Wu, C.H. Tung, T. Zhang, Facile preparation of black Nb⁴⁺ self-doped K₄Nb₆O₁₇ microspheres with high solar absorption and enhanced photocatalytic activity, *Chem. Commun.* 50 (2014) 9554–9556.
- [14] Y. Wang, X. Wang, M. Antonietti, Polymeric graphitic carbon nitride as a heterogeneous organocatalyst: from photochemistry to multipurpose catalysis to sustainable chemistry, *Angew. Chem. Int. Ed.* 51 (2012) 68–89.
- [15] E.J. Granite, M.C. Freeman, R.A. Hargis, W.J. O'Dowd, H.W. Pennline, The thief process for mercury removal from flue gas, *J. Environ. Manag.* 84 (2007) 628–634.
- [16] L. Xie, J. Ma, G. Xu, Preparation of a novel Bi₂MoO₆ flake-like nanophotocatalyst by molten salt method and evaluation for photocatalytic decomposition of rhodamine B, *Mater. Chem. Phys.* 110 (2008) 197–200.
- [17] R. Wang, X. Cai, F. Shen, TiO₂ hollow microspheres with mesoporous surface: superior adsorption performance for dye removal, *Appl. Surf. Sci.* 305 (2014) 352–358.
- [18] H. Zhang, Y. Song, Y. Sheng, H. Li, Z. Shi, X. Xu, H. Zou, EDTA-assisted fabrication of TiO₂ core-shell microspheres with improved photocatalytic performance, *Ceram. Int.* 41 (2015) 247–252.
- [19] J. Yang, Q. Yang, J. Sun, Q. Liu, D. Zhao, W. Gao, L. Liu, Effects of mercury oxidation on V₂O₅-WO₃/TiO₂ catalyst properties in NH₃-SCR process, *Catal. Commun.* 59 (2015) 78–82.
- [20] H. Li, C.Y. Wu, Y. Li, L. Li, Y. Zhao, J. Zhang, Impact of SO₂ on elemental mercury oxidation over CeO₂-TiO₂ catalyst, *Chem. Eng. J.* 219 (2013) 319–326.
- [21] F. Dong, F. Li, Q.Y. Sun, Y.J. Ho, W.K. Noble, Metal-like behavior of plasmonic Bi particles as a cocatalyst deposited on (BiO)₂CO₃ microspheres for efficient visible light photocatalysis, *ACS Catal.* 4 (2014) 4341–4350.
- [22] W.J. Wang, B.B. Huang, X.Ch. Ma, et al., Efficient separation of photogenerated electron-hole pairs by the combination of a heterolayered structure and internal polar field in pyroelectric BiOI₃ nanoplates, *Chem. Eur. J.* 19 (2013) 14777–14780.
- [23] X.M. Qi, M.L. Gu, X.Y. Zh, et al., Fabrication of BiOI₃ nanosheets with remarkable photocatalytic oxidation removal for gaseous elemental mercury, *Chem. Eng. J.* 285 (2016) 11–19.
- [24] J. Wu, X. Chen, C. Li, Y. Qi, X. Qi, J. Ren, B. Yuan, B. Ni, R. Zhou, J. Zhang, T. Huang, Hydrothermal synthesis of carbon spheres-BiOI/BiOI₃ heterojunctions for photocatalytic removal of gaseous Hg⁰ under visible light, *Chem. Eng. J.* 304 (2016) 533–543.
- [25] S. Brunauer, P.H. Emmett, E. Teller, Adsorption of gases in multimolecular layers, *J. Chem. Soc.* 60 (1938) 309–319.
- [26] J. Wu, C. Li, X. Zhao, Q. Wu, X. Qi, Photocatalytic oxidation of gas-phase Hg⁰ by CuO/TiO₂, *Appl. Catal. B* 176 (2015) 559–569.
- [27] H.W. Huang, K. Xiao, K. Liu, S.X. Yu, Y.H. Zhang, In situ composition-transforming fabrication of BiOI/BiOI₃ heterostructure: semiconductor p-n junction and dominantly exposed reactive facets, *Cryst. Growth. Des.* 16 (2016) 221–228.
- [28] H. Cheng, B. Huang, Y. Dai, X. Qin, X. Zhang, One-step synthesis of the nanostructured AgI/BiOI composites with highly enhanced visible-light photocatalytic performances, *Langmuir* 26 (2010) 6618–6624.
- [29] Y. Xu, M.A. Schoonen, The absolute energy positions of conduction and valence bands of selected semiconducting minerals, *Am. Mineral.* 85 (2000) 543–556.
- [30] M.C. Long, W.M. Cai, J. Cai, et al., Efficient photocatalytic degradation of phenol over Co₃O₄/BiVO₄ composite under visible light irradiation, *J. Phys. Chem. B* 110 (41) (2006) 20211–20216.
- [31] H. Zhang, R. Zong, J. Zhao, et al., Dramatic visible photocatalytic degradation performances due to synergetic effect of TiO₂ with PANI, *Environ. Sci. Technol.* 42 (10) (2008) 3803–3807.
- [32] F. Dong, T. Xiong, Y.J. Sun, Y.X. Zhang, Y. Zhou, Controlling interfacial contact and exposed facets for enhancing photocatalysis via 2D-2D heterostructure, *Chem. Commun.* 10 (2010) 1039.
- [33] Y. Su, L. Zhang, W.Z. Wang, Internal polar field enhanced H₂ evolution of BiOI₃ nanoplates, *Int. J. Hydrogen Energy* 41 (2016) 10170–10177.
- [34] L.B. Hou, Sh. Li, Y.H. Lin, D.J. Wang, T.F. Xie, Photogenerated charges transfer across the interface between NiO and TiO₂ nanotube arrays for photocatalytic degradation: a surface photovoltage study, *J. Colloid Interface Sci.* 465 (2016) 96–102.
- [35] L.P. Jiang, H.L. Yu, L.Y. Shi, et al., Optical band structure and photogenerated carriers transfer dynamics in FTO/TiO₂ heterojunction photocatalysts, *Appl. Catal. B* 199 (2016) 224–229.
- [36] M.Y. Guo, Alan Man Ching Ng, F.Z. Liu, et al., Photocatalytic activity of metal oxides—the role of holes and •OH radicals, *Appl. Catal. B* 107 (2011) 150–157.
- [37] Y. Yuan, Y. Zhao, H. Li, Y. Li, Electrospun metal oxide-TiO₂ nanofibers for elemental mercury removal from flue gas, *J. Hazard. Mater.* 227–228 (2012) 427–435.
- [38] K.J. Lee, C.W. Choi, W. Platinized, WO₃ as an environmental photocatalyst that generates •OH radicals under visible light, *Environ. Sci. Technol.* 44 (2010) 6849–6854.
- [39] Y. Yuan, J. Zhang, H. Li, Y. Li, Y. Zhao, C. Zheng, Simultaneous removal of SO₂, NO and mercury using TiO₂-aluminum silicate fiber by photocatalysis, *Chem. Eng. J.* 192 (2012) 21–28.